Nuclear Science and Techniques (2025) 36:62
https://doi.org/10.1007/s41365-025-01650-2

Design and verification of a new multiharmonic feedback control system for CSNS-II RCS

Jian Wu[1,2,3] · Xiang Li[1,2,3] · Bin Wu[1,3] · Yang Liu[1,3] · Chun-Lin Zhang[1,3] · Wei Long[1,3] · Jun-Yu Zhu[1,3] · Sheng-Hua Liu[1,3] · Zhi-Jun Lu[1,3] · Sheng-Yi Chen[1,3] · Xiao Li[1,3]

Received: 1 April 2024 / Revised: 9 May 2024 / Accepted: 16 May 2024 / Published online: 25 February 2025

Abstract
A dual-harmonic acceleration system is utilized to mitigate the space-charge effect in the rapid-cycling synchrotron of the China Spallation Neutron Source upgrade project (CSNS-II). A magnetic alloy (MA)-loaded cavity with a high accelerating gradient is developed to satisfy the requirements of dual-harmonic acceleration and provide the necessary second-harmonic cavity voltage. However, the MA-loaded cavity exhibits a wideband frequency response, resulting in numerous higher harmonics in the radio-frequency (RF) voltage. These higher harmonics are caused by both the beam-loading effect and distorted amplifier current, which distort the RF bucket, increase the power dissipation in the cavity, and lower the gradient. To address these issues, a multiharmonic independent feedback-control approach is implemented to compensate for higher harmonics. The effectiveness of this control strategy is validated experimentally. This study provides details regarding the feedback-control design and presents the commissioning results.

Keywords MA-loaded cavity · Beam-loading effect · Multiharmonic independent feedback control

1 Introduction

The China Spallation Neutron Source (CSNS) is a large-scale scientific facility for neutron science that provides a powerful platform for multidisciplinary application research [1]. The proton accelerator consists of an 80 MeV linac and a 1.6 GeV rapid-cycling synchrotron (RCS) [2]. The repetition frequency of the RCS is 25 Hz, and the harmonic number is two. In February 2020, a beam power of 100 kW was achieved [3].

The CSNS upgrade project (CSNS-II) has recently begun with the aim of achieving a beam power of 500 kW [4, 5]. Simultaneously, the circulating current of the RCS will increase by a factor of five [6]. The increased beam intensity will lead to a stronger space-charge effect, resulting in a larger tune shift and potential beam loss [7]. To mitigate the space-charge effect, the injection energy of the RCS in CSNS-II will be increased to 300 MeV. In addition, the RCS will incorporate a dual-harmonic acceleration system [8–10] that can enhance the bunching factor during the early acceleration stages, thereby alleviating the space-charge effect [11]. The radio-frequency (RF) system, which utilizes high-gradient magnetic alloy (MA)-loaded cavities, provides a second-harmonic ($h = 4$) voltage. Additionally, the low-Q property of the MA-loaded cavity enables a wideband frequency response, enabling it to provide both second-harmonic and fundamental voltages. Table 1 lists the main parameters of the CSNS-II/RCS.

In the context of high-intensity protons circulating in a ring, beam-loading compensation is essential for ensuring stable beam acceleration and controlling beam loss [12]. In

This work was supported by the National Natural Science Foundation of China (Nos. 11875270 and 12205317) and the Youth Innovation Promotion Association, Chinese Academy of Sciences (No. 2018015).

✉ Bin Wu
wubin@ihep.ac.cn

✉ Xiao Li
lixiao@ihep.ac.cn

1 Institute of High Energy Physics, Chinese Academy of Sciences, Beijing 100049, China

2 University of Chinese Academy of Sciences, Beijing 100049, China

3 Spallation Neutron Source Science Center, Dongguan 523803, China

Table 1 Main parameters of the CSNS-II/RCS

Parameters	Values
Circumference (m)	228
Beam power (kW)	500
Injection energy (MeV)	300
Extraction energy (GeV)	1.6
Circulating current (A)	10.73~15.29
Fundamental RF frequency (MHz)	1.72~2.44 ($h = 2$)
Beam intensity (ppp)	7.80×10^{13}
Cavity number	8 ferrite-loaded cavities
	+ 3 MA-loaded cavities
Maximum RF voltage	175 kV($h = 2$) + 100 kV($h = 4$)

addition to the accelerating harmonic, the wide spectrum of the beam current and nonlinearity of the tetrode tubes used as final amplifiers generate rich higher harmonics in the wideband MA-loaded cavity. Failure to compensate for these undesired harmonics can result in bucket distortion and emittance growth [13–15]. Therefore, both the beam-loading effect and nonlinearity of the RF amplifier must be carefully considered in a wideband system, and multi-harmonic compensation must be implemented to address these issues. Since the nonlinearity of the tubes negatively affects the performance of the feedforward method [16], extensive investigations have been conducted on multiharmonic feedback-control systems to address the undesired harmonics from both beam loading and the nonlinearity of RF amplifiers.

The MA-loaded cavity is divided into upstream and downstream sections. The vector control of the vector sum voltage of the upstream and downstream sections has been reported [17]. However, it does not completely eliminate unwanted harmonics in either section driven by a pair of tetrode tubes working in push–pull mode. These harmonics do not contribute to beam acceleration, but result in extra power dissipation in the cavity. Therefore, an independent control configuration is employed to control the cavity voltage in the upstream and downstream sections. This approach enables the suppression of unwanted harmonics, thereby minimizing power dissipation and achieving a higher gradient.

The remainder of this paper is organized as follows. Section 2 presents a brief overview of the RF system configuration, which lays the groundwork for understanding the technical environment in which our solution operates. A comprehensive description of the design methodology and framework for multiharmonic independent feedback control, detailing the new approach we have taken to address the challenges identified, will be provided in Sect. 3. Section 4 validates the feasibility of our proposed algorithm through beam experiments, demonstrating its effectiveness in a practical setting.

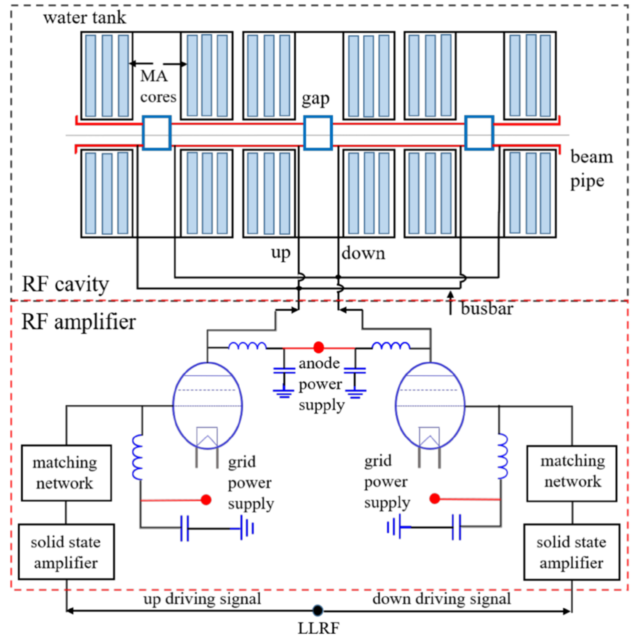

Fig. 1 (Color online) Schematic of the MA-loaded cavity

2 RF system

2.1 RF cavity

The MA-loaded cavity has a length of 1.8 m. It contains six water tanks, each of which consists of three MA cores of size $\Phi\,850\,\mathrm{mm}\times316\,\mathrm{mm}\times25\,\mathrm{mm}$, forming three acceleration gaps. All the gaps are connected in parallel through the busbars. A schematic of the cavity is shown at the top of Fig. 1; the materials, manufacturing process, and performance tests of the cavity are described in detail in [18, 19]. The cavity is partitioned into upstream and downstream sections. The gap voltage is the vector sum voltage of the upstream and downstream sections, which represents the voltage difference between them. This serves as the accelerating voltage experienced by the beam as it passes through the acceleration gap.

The design of the Q-value and resonant frequency of the RF cavity follows the method outlined in [20]. This design approach aims to minimize the amplifier current, resulting in a Q-value of approximately 1.3 and resonant frequency of 2.1 MHz. Figure 2 shows the cavity impedance, which clearly demonstrates the wideband characteristics of the cavity. The maximum cavity impedance is approximately 200 Ω.

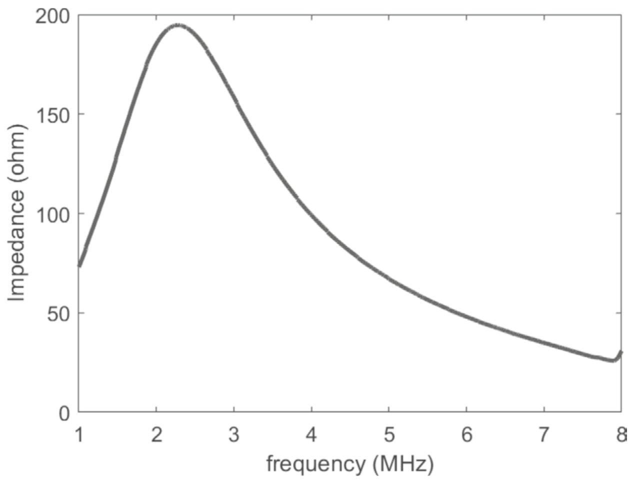

Fig. 2 (Color online) Measured impedance of the MA-loaded cavity

2.2 RF amplifier

The RF signal-amplifier chain consists of two solid-state amplifiers (SSA) and a final-stage amplifier equipped with two TH558 tetrode tubes. The low-level RF (LLRF) control system generates an RF-driven signal that is directed to the SSA. The SSA output drives the control grid of the tetrode tubes. The tubes adopt a grounded-cathode structure and are powered by an anode power supply. Each tube is connected to the gaps using busbars. The two tubes form a push–pull configuration. A simplified schematic of the RF power system is shown at the bottom of Fig. 1.

The tubes are operated in Class AB with a conduction angle greater than 180°. Consequently, the tube current is cut off during a portion of each cycle. Because of this distortion and the wideband property of the cavity, the cavity voltage driven by the tube current exhibits several harmonics. This will be discussed in the next section. A multiharmonic feedback control is employed in LLRF to address these higher harmonics.

3 Analysis and design of the multiharmonic feedback control

3.1 Independent RF voltage control

Numerous reports have confirmed that one of the greatest advantages of MA-loaded cavities is their high-gradient capability, which is effectively demonstrated through the push–pull operating mode [21, 22]. However, as discussed in the previous sections, their wideband characteristics can lead to the excitation of a multitude of higher-order harmonic voltages, thereby making the suppression of unwanted harmonics a primary task for the LLRF control system. Traditional control algorithms that utilize signals synthesized from the vector sum of the voltages across the gap can effectively suppress the beam-induced harmonics and odd harmonics generated by the tube [17]. However, they fall short of addressing the even-order harmonics produced by the tube. These unsuppressed harmonics can lead to increased cavity power dissipation, thereby limiting the further enhancement of the gradient of the MA-loaded cavity. The following provides a detailed explanation for this phenomenon.

According to [23], the anode currents in the two tubes in a push–pull configuration have the following cosine pulse forms:

$$
\begin{aligned}
y^A &= \begin{cases} A(\cos\phi - \cos\alpha), & -\alpha < \phi < \alpha \\ 0, & -\pi < \phi < -\alpha, \alpha < \phi < \pi \end{cases} \\
y^B &= \begin{cases} A(\cos(\phi+\pi) - \cos\alpha), & -\alpha-\pi < \phi < \alpha-\pi \\ 0, & -2\pi < \phi < -\alpha-\pi, \alpha-\pi < \phi < 0. \end{cases}
\end{aligned} \tag{1}
$$

Here, A is the amplitude, and α is the conduction angle. We can perform a Fourier series expansion of Eq. (1) to calculate the harmonic components. The equations for the harmonic components are as follows:

$$
\begin{aligned}
I_n^A &= \frac{1}{\pi}\int_{-\alpha}^{\alpha} A(\cos\phi - \cos\alpha)\cos(n\phi)\mathrm{d}\phi \\
Q_n^A &= \frac{1}{\pi}\int_{-\alpha}^{\alpha} A(\cos\phi - \cos\alpha)\sin(n\phi)\mathrm{d}\phi
\end{aligned} \tag{2}
$$

$$
\begin{aligned}
I_n^B &= \frac{1}{\pi}\int_{-\alpha}^{\alpha} A(\cos\theta - \cos\alpha)\cos(n(\theta-\pi))\mathrm{d}\theta \\
Q_n^B &= \frac{1}{\pi}\int_{-\alpha}^{\alpha} A(\cos\theta - \cos\alpha)\sin(n(\theta-\pi))\mathrm{d}\theta,
\end{aligned} \tag{3}
$$

where I_n and Q_n are the cosine and sine coefficients of the n^{th} harmonic, respectively. By comparing Eq. (2) and Eq. (3), we observe that

$$
I_n^A = \begin{cases} -I_n^B, n = \text{odd} \\ I_n^B, n = \text{even} \end{cases} \quad Q_n^A = \begin{cases} -Q_n^B, n = \text{odd} \\ Q_n^B, n = \text{even}. \end{cases} \tag{4}
$$

This suggests that the odd-order harmonics of the anode current between the two tubes are antiphase, whereas the even-order harmonics are in phase. Consequently, owing to the push–pull configuration, the even harmonics in both the upstream and downstream signals are inherently canceled out in the vector-sum signal.

Figure 3 shows the measured voltage waveforms of the upstream and downstream sections, and their vector sum. The driving signal is a pure sinusoidal wave. The voltages in the upstream and downstream sections are distorted because of the presence of several harmonics. According to the FFT results, the fundamental, second, and third harmonics in

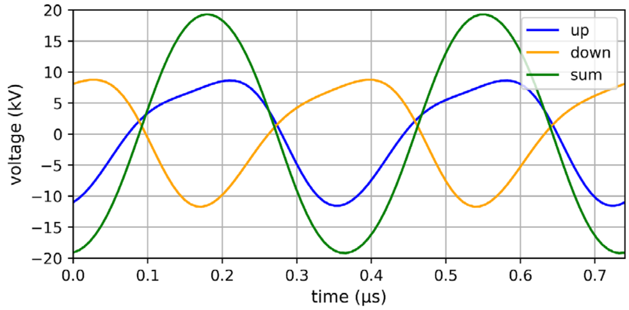

Fig. 3 (Color online) Cavity-voltage waveform of upstream (blue), downstream (orange), and the vector-sum voltage (green)

both sections are approximately 9.8 kV, 2.2 kV, and 0.25 kV, respectively. The other harmonics are negligible. In contrast, the vector-sum voltage exhibits few harmonic components. The fundamental, second, and third harmonics are 19.6 kV, 0.211 kV, and 0.408 kV, respectively.

Traditional vector-control algorithms face challenges in suppressing even-order harmonics. The existence of even harmonics in both the upstream and downstream sections does not contribute to beam acceleration because the beam only experiences the vector-sum voltage. Instead, their practical existence leads to an increase in power dissipation within the cavity, causing the temperature of the magnetic cores to further increase. This is particularly problematic when the cavity operates at a high duty cycle, which can hinder further improvements in the cavity gradient owing to the limitations imposed by the maximum temperature of the MA cores [19, 24].

Based on this, we propose an algorithm for independent control that refers to the separate regulation of voltage in the upstream and downstream gaps. In this approach, the upstream and downstream RF voltages are detected by sampling capacitors and then input into the feedback module for individual regulation. The output of the feedback module drives two amplifiers that supply currents to the upstream and downstream sections. The independent control method can effectively suppress the higher harmonics in both the upstream and downstream sections, leading to reduced power dissipation in the cavity. In addition, this enables the attainment of higher field gradients.

In the following section, we evaluate the effects of these two control algorithms on the power dissipation of the cavity using the data presented in Figs. 2 and 3.

The fundamental frequencies shown in Fig. 3 are approximately 2.75 MHz. In Fig. 2, the impedances at the fundamental and second-harmonic frequencies are approximately 175 Ω and 60 Ω, respectively. The power dissipated by the second-harmonic accounts for approximately 14.6% of the total power. Compared with vector control, independent control can compensate for the second harmonic in both the upstream and downstream sections; therefore, an increase of approximately 1.6 kV in the fundamental harmonic of each gap (4.8 kV for a cavity because of three gaps) can be achieved with the assumption of the same total power dissipation for both control algorithms. This approach is meaningful for endeavors aimed at achieving high-gradient operations.

Therefore, independent voltage control is implemented to minimize the cavity power and achieve a higher gradient.

3.2 Consideration for A/ϕ and I/Q control

In terms of voltage regulation, an RF signal can be represented by its amplitude and phase (A/ϕ) or by its in-phase and quadrature-phase (I/Q) components; thus, both the A/ϕ and I/Q control methods can be employed. Although both methods have proven effective, their advantages and disadvantages must be carefully examined to achieve optimal performance [25].

The stability and reliability of the A/ϕ control in the LLRF system for the CSNS/RCS has been demonstrated [26]. However, compensating for the heavy beam loading in the MA-loaded cavity requires setting the setpoint to zero, resulting in a very small-amplitude signal output by the A/ϕ control. This causes an unstable phase loop, rendering it unsuitable for MA-loaded cavity-voltage regulation. By contrast, the I/Q loop delivers superior performance in low-amplitude scenarios because it can be driven negatively [27]. Therefore, an I/Q feedback-control structure is under consideration.

3.3 Loop-phase calibration for I/Q control

In the context of I/Q control, loop-phase calibration is required because a substantial loop phase can introduce significant crosstalk between the I/Q channels, potentially leading to instability in I/Q control. Throughout this study, the loop phase refers to the phase response of the feedback loop from the I/Q modulator to the demodulator. The primary contributors to the loop phase are the loop delay and frequency response of the cavity and analog devices. The impact of the loop phase on the feedback is crucial for I/Q control.

To illuminate the impact of the loop phase on feedback, [28] provides an analysis of a scenario in which a loop phase of 180° results in feedback instability, as depicted in Fig. 4. Owing to the large loop phase, after feedback correction, the cavity field is modified but moves in the opposite direction to the set point.

While analyzing the I/Q control for a more general case with an arbitrary loop phase, we observed that instability may also occur. This can be explained through the following analysis.

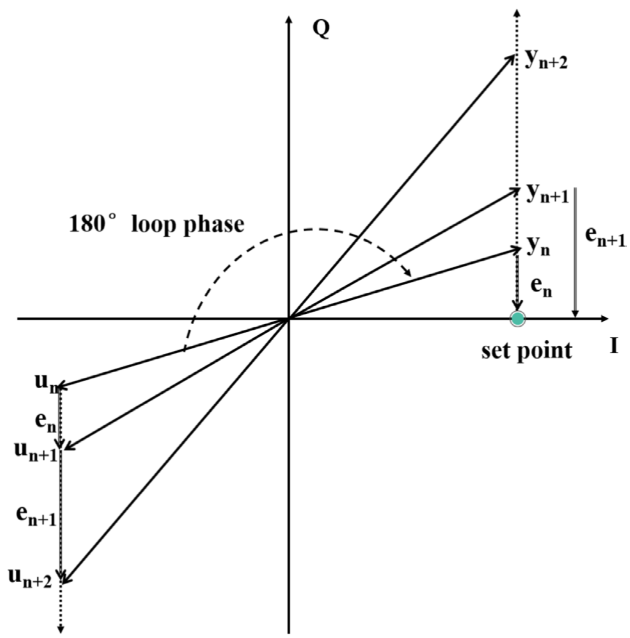

Fig. 4 (Color online) Example of feedback instability of the I/Q control with a loop phase of 180°

The current cavity field, denoted as y_n, can be expressed as follows:

$$\begin{bmatrix} y_{In} \\ y_{Qn} \end{bmatrix} = R\begin{bmatrix} u_{In} \\ u_{Qn} \end{bmatrix} = R\begin{bmatrix} u_{I,n-1} \\ u_{Q,n-1} \end{bmatrix} + G\begin{bmatrix} e_{I,n-1} \\ e_{Q,n-1} \end{bmatrix}. \tag{5}$$

Here, G represents the loop gain, and R is the rotation matrix that depends on the loop phase. The variables u and e represent the control signal and error, respectively. R is expressed as follows:

$$R = \begin{bmatrix} \cos\theta & \sin\theta \\ -\sin\theta & \cos\theta \end{bmatrix}. \tag{6}$$

We can further rewrite (5) as follows:

$$\begin{aligned} \begin{bmatrix} y_{In} \\ y_{Qn} \end{bmatrix} &= \begin{bmatrix} y_{I,n-1} \\ y_{Q,n-1} \end{bmatrix} + RG\begin{bmatrix} set_I - y_{I,n-1} \\ set_Q - y_{Q,n-1} \end{bmatrix} \\ &= RG\begin{bmatrix} set_I \\ set_Q \end{bmatrix} + (I - RG)\begin{bmatrix} y_{I,n-1} \\ y_{Q,n-1} \end{bmatrix}. \end{aligned} \tag{7}$$

In general, the cavity field converges if (8) is satisfied.

$$|EIG(I - RG)| < 1 \tag{8}$$

Therefore, the cavity field can be regulated to the set point, as indicated by (9).

$$\begin{bmatrix} y_{In} \\ y_{Qn} \end{bmatrix} = (RG)^{-1} \cdot RG\begin{bmatrix} set_I \\ set_Q \end{bmatrix} = \begin{bmatrix} set_I \\ set_Q \end{bmatrix} \tag{9}$$

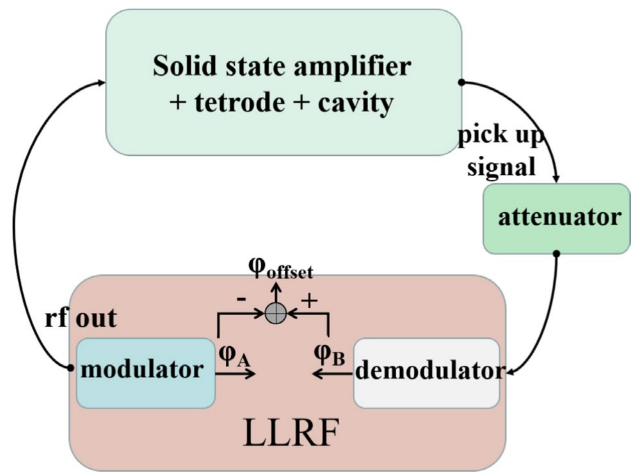

Fig. 5 (Color online) Loop-phase measurement method

The maximum allowable loop phase in the feedback loop is determined by the loop gain. Higher loop gains necessitate smaller loop phases to preserve stability. Consequently, calibrating the loop phase to a minimum value is advantageous, guaranteeing feedback stability and enhancing the feedback gain. This, in turn, contributes to a reduction in set-point tracking errors.

The loop phase is measured and calibrated using an open loop, as shown in Fig. 5. ϕ_A represents the initial phase of the RF signal prepared by the modulator, and ϕ_B in the demodulator includes the phase response of the feedback loop. The loop phase (denoted by ϕ_{offset}) is obtained as ϕ_B-ϕ_A. After calibration, a new RF signal is generated as follows:

$$rf = I \cdot \sin(2\pi f_n t + \phi_A - \phi_{\text{offset}}). \tag{10}$$

If ϕ_{offset} is measured accurately, the result of the loop phase is zero.

Separate calibrations were performed for each harmonic. Calibration of the loop phase was performed up to ($h = 8$); however, only the loop phases for ($h = 2$) and ($h = 4$) are shown in Fig. 6 for clarity. ϕ_{offset} varies continuously with frequency. As indicated in the lower part of Fig. 6, a linear relationship exists between ϕ_{offset} and the frequency, indicating that the primary cause of the loop phase is delay.

The ϕ_{offset} value for each harmonic is stored in the memory of a field-programmable gate array (FPGA) as a phase pattern. After calibration, the ϕ_{offset} values for all harmonics are close to zero, as shown in Fig. 7. At this stage, the feedback loops can be closed owing to successful calibration.

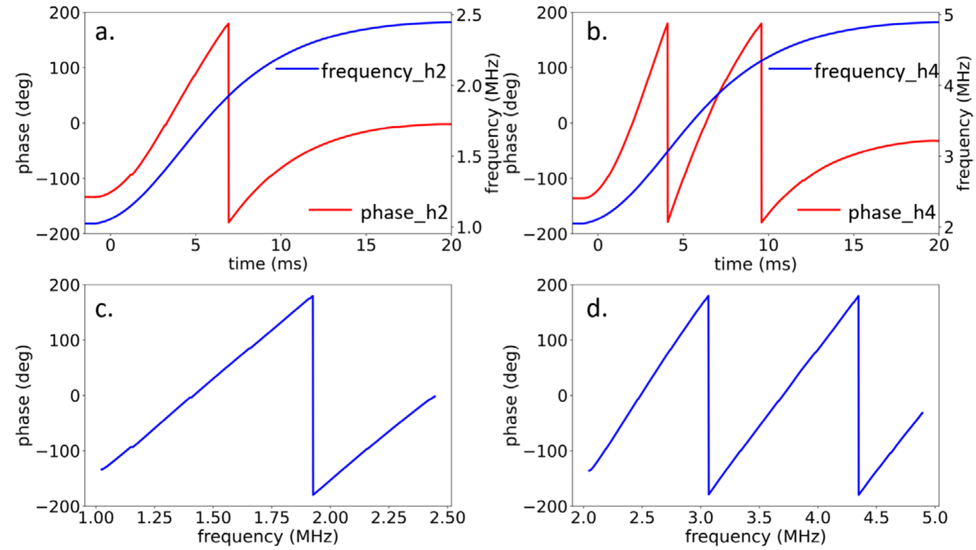

Fig. 6 (Color online) (a) Loop phase and frequency of ($h = 2$) versus time. (b) Loop phase and frequency of ($h = 4$) versus time. (c) Loop phase versus frequency ($h = 2$). (d) Loop phase versus frequency ($h = 4$)

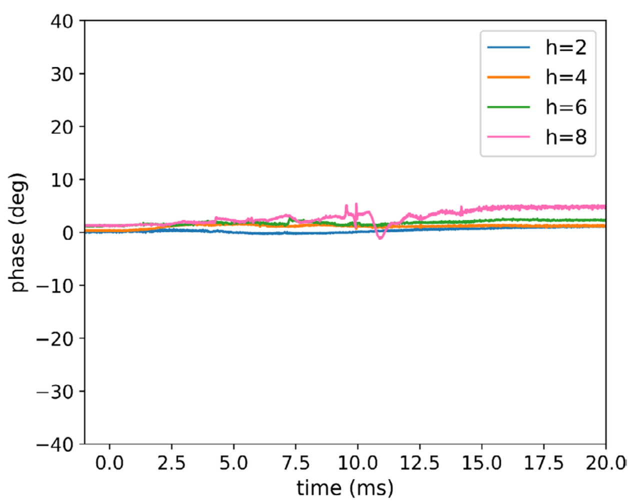

Fig. 7 (Color online) All values of ϕ_{offset} for harmonics after calibration

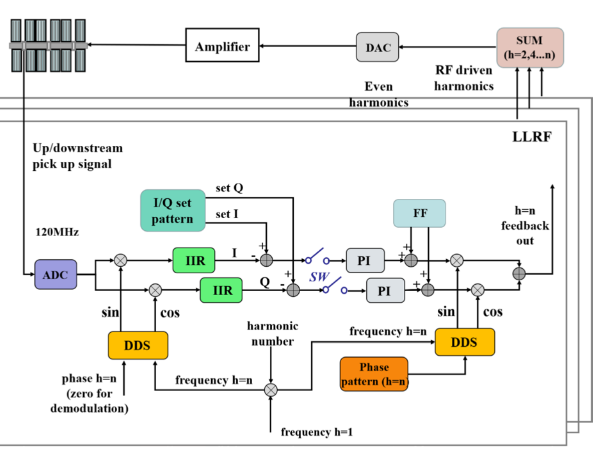

Fig. 8 (Color online) Block diagram of the multiharmonic feedback control

3.4 Multiharmonic feedback control

Figure 8 shows a simplified block diagram of the multiharmonic feedback-control system. To enable feedback control and monitoring, sampling capacitors are strategically placed in the upstream and downstream sections. The pickup signal is then converted into a digital signal using a high-speed analog-to-digital converter operating at a clock frequency of 120 MHz. The digital signal is subsequently directed to the feedback block of each harmonic.

A direct digital synthesizer (DDS) is used to generate sine and cosine signals of unity amplitude with a highly accurate frequency. The frequency signal ($h = n$) fed to the DDS is obtained by multiplying the revolution frequency ($h = 1$) by the selected harmonic number. For demodulation, the phase signal ($h = n$) fed into the DDS is zero, whereas for modulation, it is derived from the phase pattern. The phase pattern stores the phase offset (ϕ_{offset}) obtained from the loop-phase calibration in Sect. 3.3. The feedforward (FF) module is used for open-loop measurements.

The low-pass filter, which facilitates the acquisition of the I/Q values of the selected harmonic from the mixed signals, plays a critical role in the feedback control. The filter must have sufficient bandwidth to enable a fast feedback response while also being narrow enough to reject other harmonics. Additionally, the delay and FPGA-logic requirements should be considered. In our implementation, we utilized a second-order infinite impulse-response low-pass filter to circumvent the significant delay associated with high-order finite impulse-response filters. The filter has a bandwidth of approximately 60 kHz and provides rejection at the 80 dB level at frequencies above 500 kHz.

The I/Q errors are continuously updated by comparing the I/Q values with the designated I/Q set points and are subsequently minimized by the feedback controller. Although various new feedback controllers have been reported, such as the linear quadratic regulator [29, 30] and model predictive control [31], we chose to use a proportional and integral (PI) controller. This decision was based on the challenges associated with obtaining the model of an RF system operating in sweeping mode, which is crucial for controllers relying on the system model, as well as the advantages of simplicity, robustness, and easy parameter tuning associated with the PI controller. The PI values were carefully selected to achieve satisfactory tracking performance in the presence of disturbances, while simultaneously maintaining low levels of high-frequency noise.

In addition, to provide flexibility, the harmonic feedback loop includes a switch that allows the closing or opening of the feedback loop.

The RF-driven signal is formed by summing all feedback output signals, which are then prepared by the I/Q modulator. Finally, the driven signal is converted back to an analog signal using a digital-to-analog converter and transmitted to the amplifier chain.

4 Experimental results

4.1 Beam-off experiments

Prior to the official implementation of the multiharmonic feedback control, an assessment was conducted to reduce the voltage-waveform distortion caused by the nonlinearity of the RF amplifiers.

The selected driven harmonic is ($h = 2$), with the programmed voltage and frequency patterns matching those used during operation. Figure 9(a) presents the harmonic components of the upstream cavity voltage when only the feedback for ($h = 2$) is closed. The voltage amplitude for ($h = 2$) is effectively regulated at 5 kV. The primary observed harmonic component is the 2$^{\text{nd}}$ harmonic, which reaches a maximum amplitude of approximately 2.2 kV. Additionally, a small amount of the 3$^{\text{rd}}$ and 4$^{\text{th}}$ harmonic components exist, both measuring less than 0.3 kV. Owing to the tube operation (class AB1) and cavity frequency response, the other higher-order harmonics exhibit minimal components.

Further closure of the feedback loops for ($h = 4, 6, 8$), with ($I_{\text{set}}, Q_{\text{set}}$) set to (0, 0) as the set points, effectively suppresses the higher harmonics, as shown in Fig. 9(b). The fundamental harmonic remains the same, whereas the 2$^{\text{nd}}$ harmonic is reduced from 2.2 kV to 0.15 kV, and the other harmonics are below 0.1 kV. After compensating for the higher harmonics, the cavity power is reduced from 40 kW to 36 kW.

The experimental results confirmed the functionality of the multiharmonic I/Q feedback control. The even harmonics in both streams were successfully reduced by independent control, resulting in a significant decrease in cavity-power dissipation.

4.2 Beam-loading compensation

With the beam commissioning for dual-harmonic acceleration, the MA-loaded cavity was successfully operated, providing both fundamental and second-harmonic voltages. The following experimental results further validate the effectiveness of multiharmonic feedback control under the beam-loading effect.

Initially, the beam loading in the MA-loaded cavity is measured at a beam intensity of 1.95×10^{13} protons per pulse (ppp) for two bunches, corresponding to a beam power of 125 kW. The wake voltages are shown in the upper graphs in Fig. 10(a). During this phase, no feedback control is applied to any of the harmonics. The MA-loaded cavity does not supply RF voltage, and the accelerating voltage is provided by the ferrite-loaded cavities. The injection pulse width is 514 μs.

Only even harmonics are observed in the gap voltage because two bunches are accelerated. The maximum amplitudes of the 1$^{\text{st}}$ ($h = 2$), 2$^{\text{nd}}$, and 3$^{\text{rd}}$ harmonics of the wake voltage in one gap between the injection and extraction are approximately 8 kV, 2 kV, and 1 kV, respectively. The slight

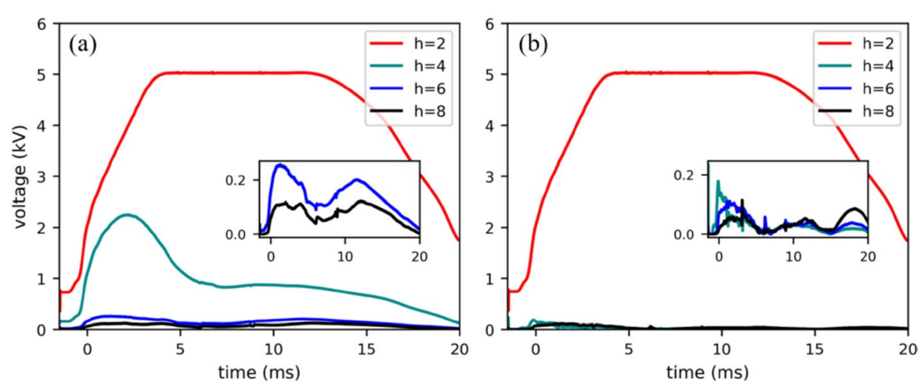

Fig. 9 (Color online) Harmonic components of upstream voltage in the case of (a) the feedback closed for ($h = 2$) only and (b) the feedback loops closed for ($h = 2, 4, 6, 8$)

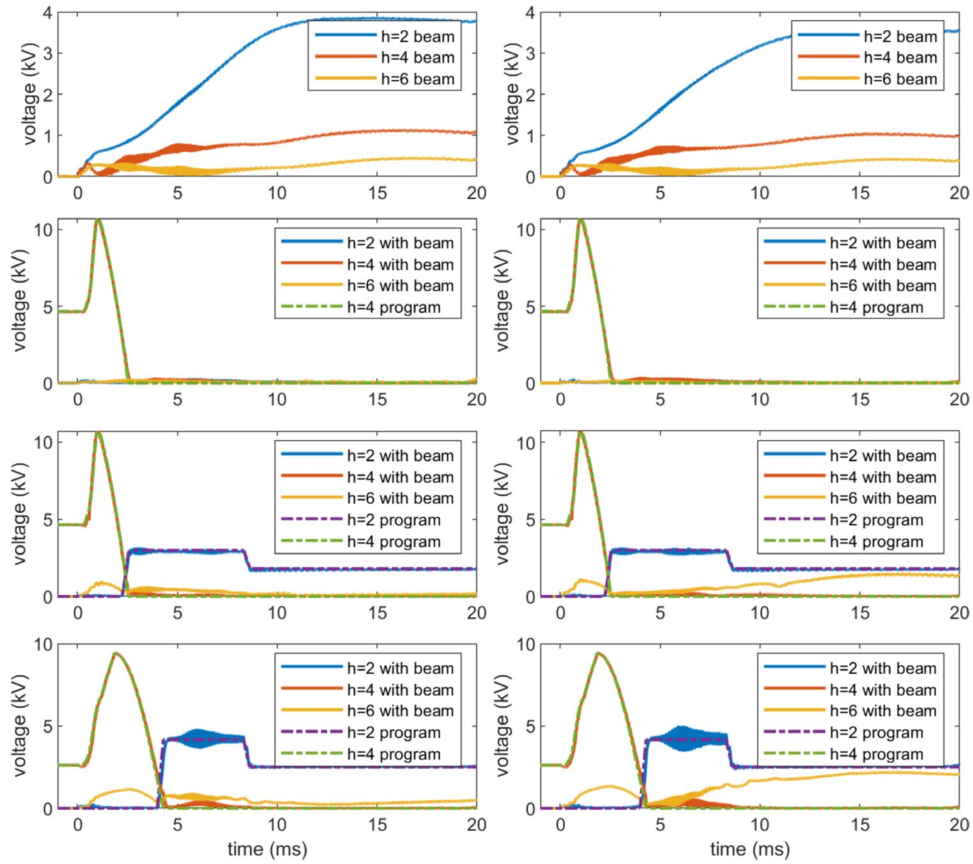

Fig. 10 (Color online) Harmonic components of the wake voltage of 125 kW beam at both ends of one gap without feedback (a). Harmonic components of the voltage at both ends of one gap with the acceleration of a 125 kW beam with feedback for ($h = 2, 4, 6$) (b). Harmonic components of the voltage at both ends of one gap with the acceleration of a 140 kW beam with feedback for ($h = 2, 4$) (c). Harmonic components of the voltage at both ends of one gap with the acceleration of a 160 kW beam with feedback for ($h = 2, 4$) (d). The left and right plots show the RF voltages at the upstream and downstream ends of one gap, respectively

discrepancies in wake voltages between the upstream and downstream sections can be attributed to minor manufacturing differences between the MA cores housed within the tanks.

Next, the LLRF system generates an RF signal for the MA-loaded cavity. In this scenario, the RF signal is composed of the driving signal for beam acceleration and the compensation signal for beam-loading compensation. The performance of the MA-loaded cavity supplying a maximum ($h = 4$) second-harmonic voltage of approximately 66 kV (11 kV for each end) under 125 kW beam loading is tested with feedback for ($h = 2, 4, 6$). The beam test results are shown in Fig. 10(b). With feedback, the second-harmonic voltage is well regulated according to the voltage program from the beginning to 2.5 ms. After 2.5 ms, the second-harmonic voltage is effectively suppressed below 0.3 kV. The ($h = 2$) beam loading is effectively mitigated, decreasing from 4 kV to 0.4 kV, and the ($h = 6$) harmonic is consistently suppressed below 0.4 kV throughout the cycle.

A beam power of 140 kW is achieved [32] with successful beam commissioning. The voltage program for the 140 kW beam acceleration and harmonic components of ($h = 2, 4, 6$) in the upstream and downstream sections are shown in Fig. 10(c). Given the small size above the ($h = 6$) harmonic during beam acceleration [33], feedback is applied only for ($h = 2, 4$) in the beam commission. The ($h = 4$) harmonic remains well regulated at 11 kV according to the voltage pattern. In addition to the ($h = 4$) harmonic voltage, the MA-loaded cavity also features an ($h = 2$) harmonic-voltage program from 2 ms to 20 ms with a maximum of 18 kV (3 kV for each end), aimed at reducing beam loss in the arc region and alleviating beam instability. The ($h = 2$) harmonic is maintained well below 0.35 kV during the initial 2 ms to 20 ms. However, some oscillations occur in the ($h = 2$) voltage range from 3 ms to 8 ms, which are likely caused by the longitudinal oscillation of the beam and are currently under investigation. However, this does not result in a significant beam-intensity loss.

After the installation of an additional MA-loaded cavity, the beam power has recently been increased to 160 kW. Each MA-loaded cavity provides both ($h = 2$) and ($h = 4$) harmonic voltages with a voltage program that differs from that used for the 140 kW beam acceleration. Each cavity delivers a maximum (h=4) harmonic voltage of 50 kV from the beginning to 4 ms and provides a ($h = 2$) harmonic voltage of 25 kV from 4 ms to 20 ms, as shown in Fig. 10(d). The performance of the ($h = 4$) harmonic-voltage regulation has not deteriorated despite the heavier beam loading and is well regulated throughout the entire acceleration cycle, with a maximum deviation of 0.5 kV at approximately 6.5 ms. However, the oscillations in the ($h = 2$) voltage have increased, with the amplitude reaching 1 kVpp. These oscillations also align with changes in the voltage program. They do not significantly impact the beam acceleration at the current stage; however, we plan to implement an adaptive feedforward control based on the approach described in [34] to enhance the tracking performance.

The disparity in the (h=6) harmonics between the upstream and downstream sections is observed in Fig. 10(c) and (d). This discrepancy occurs because the harmonics stem not only from the wake voltage, but also from the distorted tube output current, as the two tube output current waveforms exhibit asymmetry under beam-loading effects [35]. This characteristic is inherent to multiharmonic operations. Despite the different tube operating conditions, the feedback demonstrates effective functionality in all cases.

5 Summary

We devised a multiharmonic independent voltage feedback control for a wideband RF system for the CSNS-II. A control configuration and feedback block diagram are presented. We conducted comprehensive experiments to assess the feedback-control performance. The simultaneous regulation of multiple harmonics in a cavity under 160 kW beam loading was achieved. However, the longitudinal behavior of beam-induced oscillations in the RF voltage has not yet been addressed. Further improvements in the control algorithm are required. A system-level tetrode model encompassing beam-loading effects and feedback-control functionalities is currently being developed and has received initial validation based on LTspice. Subsequently, we will utilize this model to assess the feasibility of the proposed independent control algorithm under conditions of higher beam power operation.

Author contributions All authors contributed to the study conception and design. Material preparation, data collection, and analysis were performed by Jian Wu, Xiang Li, Bin Wu, and Xiao Li. The first draft of the manuscript was written by Jian Wu, and all authors commented on the previous versions of the manuscript. All authors read and approved the final manuscript.

Data availability The data that support the findings of this study are openly available in Science Data Bank at https://cstr.cn/31253.11.sciencedb.j00186.00493 and https://www.doi.org/10.57760/sciencedb.j00186.00493

Declarations

Conflict of interest The authors declare that they have no conflict of interest.

References

1. J. Wei, S.N. Fu, J.Y. Tang et al., China spallation neutron source - an overview of application prospects. Chin. Phys. C **33**, 1033 (2009). https://doi.org/10.1088/1674-1137/33/11/021
2. S. Wang, S.X. Fang, S.N. Fu et al., Introduction to the overall physics design of CSNS accelerators. Chin. Phys. C **33**, 1 (2009). https://doi.org/10.1088/1674-1137/33/S2/001
3. S.Y. Xu, H.Y. Liu, J. Peng et al., Beam commissioning and beam loss control for CSNS accelerators. J. Instrum. **15**, 07 (2020). https://doi.org/10.1088/1748-0221/15/07/P07023
4. J. Zhang, S.N. Fu, H.S. Chen et al., Status of CSNS Project. Paper presented at the Proceedings of the 2nd International Symposium on Science, Ibaraki, Japan, 012005 July 2014. https://doi.org/10.7566/JPSCP.8.012005
5. J. Wei, H. Chen, Y. Chen et al., China Spallation Neutron Source: Design, R &D, and outlook. Nucl. Instrum. Methods Phys. Res. Sect. Accel. Spectrometers Detect. Assoc. Equip. **600**, 10–13 (2009). https://doi.org/10.1016/j.nima.2008.11.017
6. S.N. Fu, S. Wang, Operation status and upgrade of CSNS. in: 2009 International Particle Accelerator Conference (IPAC). 23–27 (2019). https://doi.org/10.18429/JACoW-IPAC2019-MOZPLM1
7. S.Y. Xu, S. Wang, Study on space charge effects of the CSNS/RCS. Chin. Phys. C **35**, 1152 (2011). https://doi.org/10.1088/1674-1137/35/12/014
8. J.F. Chen, J.Y. Tang, Studies of dual-harmonic acceleration at CSNS. Chin. Phys. C **34**, 1643 (2010). https://doi.org/10.1088/1674-1137/34/10/018
9. Y.S. Yuan, N. Wang, S.Y. Xu et al., Theoretical study of a dual harmonic system and its application to the CSNS/RCS. Chin. Phys. C **39**, 127002 (2015). https://doi.org/10.1088/1674-1137/39/12/127002
10. H.Y. Liu, S. Wang, Longitudinal beam dynamic design of 500 kW beam power upgrade for CSNS-II RCS. Radiat. Detect. Technol. Methods **6**, 339–348 (2022). https://doi.org/10.1007/s41605-022-00325-5
11. A. Seville, D. Adams, C. Appelbee et al., Progress on dual harmonic acceleration on the ISIS synchrotron. in: 2007 IEEE particle accelerator conference (PAC). 1649–1651 (2007). https://doi.org/10.1109/PAC.2007.4440852
12. F. Pedersen, Beam loading effects in the CERN PS booster. IEEE T. Nucl. Sci **22**(3), 1649–1651 (1975). https://doi.org/10.1109/TNS.1975.4328024
13. K. Saito, M. Fujieda, Y. Mori et al., Higher harmonics beam loading compensation for a broad band MA-loaded RF cavity. No. KEK-98-80. SCAN-9809016, 1998. https://api.semanticscholar.org/CorpusID:6846765
14. M. Yamamoto, Longitudinal particle tracking code for a high intensity proton synchrotron. in: 2016 ICFA Advanced Beam Dynamics Workshop on High-Intensity and High-Brightness Hadron Beams (HB). 110–114 (2016). https://doi.org/10.18429/JACoW-HB2016-MOPR022
15. B. Wu, H. Sun, X. Li et al., Higher harmonic voltage analysis of magnetic-alloy cavity for CSNS/RCS upgrade project. Radiat. Detect. Technol Methods **4**, 293–302 (2022). https://doi.org/10.1007/s41605-020-00183-z
16. F. Tamura, M. Yamamoto, C. Ohmori et al., Multiharmonic RF feedforward system for beam loading compensation in wideband cavities of a rapid cycling synchrotron. Phys. Rev. Accel. Beams **14**, 051004 (2011). https://doi.org/10.1103/PhysRevSTAB.14.051004
17. F. Tamura, Y. Sugiyama, M. Yoshii et al., Multiharmonic vector rf voltage control for wideband cavities driven by vacuum tube amplifiers in a rapid cycling synchrotron. Phys. Rev. Accel.

Beams **22**, 092001 (2019). https://doi.org/10.1103/PhysRevAccelBeams.22.092001
18. B. Wu, X. Li, Z. Li et al., Development of a large nanocrystalline soft magnetic alloy core with high μQf products for CSNS-II. Nucl. Sci. Tech. **33**, 99 (2022). https://doi.org/10.1007/s41365-022-01087-x
19. B. Wu, X. Li, C.L. Zhang et al., Design and verification of a high-gradient and high-power 2nd harmonic cavity for the China Spallation Neutron Source upgrade project. Rev. Sci. Instrum. **94**, 043301 (2023). https://doi.org/10.1063/5.0141079
20. M. Yamamoto, M. Nomura, A. Schnase et al., Dual harmonic acceleration with broadband MA cavities in J-PARC RCS. In: 2004 European Particle Accelerator Conference (EPAC). 1318–1320 (2004)
21. C. Ohmori, E. Ezura, M. Fujieda et al., High field-gradient cavities loaded with magnetic alloys for synchrotrons. In: 1999 Particle Accelerator Conference (PAC). 413–417 (1999). https://doi.org/10.1109/PAC.1999.795720
22. C. Ohmori, E. Ezura, M. Fujieda et al., Development of high gradient RF system for J-PARC upgrade. in: 2015 International Particle Accelerator Conference (IPAC). 50–52 (2015). https://doi.org/10.18429/JACoW-IPAC2015-MOAD1
23. H.Y. Qian, Analysis and design of CMOS radio-frequency power amplifiers. Doctoral dissertation, Texas A & M University. Available electronically from https://hdl.handle.net/1969.1/161560
24. T. Shimada, M. Nomura, F. Tamura et al., Measurement of thermal deformation of magnetic alloy cores of radio frequency cavities in 3-GeV rapid-cycling synchrotron of Japan proton accelerator research complex. Nucl. Instrum. Meth. A **875**, 92–103 (2017). https://doi.org/10.1016/j.nima.2017.08.039
25. T. Olof, Cavity field control for linear particle accelerators. Diss. Lund University, 2019, Chapter 10, pp. 129. https://lup.lub.lu.se/search/files/71528958/thesis_troeng.pdf
26. X. Li, H. Sun, W. Long et al., Design and performance of the LLRF system for CSNS/RCS. Chin. Phys. C **39**, 2 (2015). https://doi.org/10.1088/1674-1137/39/2/027002
27. A. Seville, D.B. Allen, Progress on the ISIS synchrotron digital low level RF system upgrade. arxiv preprint arxiv:1910.07302 (2019). https://doi.org/10.48550/arXiv.1910.07302
28. B. Alexander, Development of a Finite State Machine for the Automated Operation of the LLRF Control at FLASH. No. DESY-THESIS–2007-024. Deutsches Elektronen-Synchrotron (DESY), Chapter 4, pp. 76 (2007). https://doi.org/10.3204/DESY-THESIS-2007-024
29. A. Martin, Modelling, Control and Stability Analysis of an RF Cavity in CERN LINAC4. Diss. Aalborg U., Chapter 4, pp. 44 (2020). https://cds.cern.ch/record/2721829
30. R. Büchi, *State Space Control LQR and Observer: step by step introduction, with Matlab examples* (Books on Demand, 2010)
31. M. Nikolao, Model predictive controllers: a critical synthesis of theory and industrial needs. Adv. Chem. Eng. **26**, 131–204 (2001). https://doi.org/10.1016/S0065-2377(01)26003-7
32. J. Wu, X. Li, B. Wu et al., Design and commissioning of a wideband RF system for CSNS-II rapid-cycling synchrotron. Nucl. Sci. Tech. **35**, 5 (2024). https://doi.org/10.1007/s41365-024-01377-6
33. H. Liu, L.S. Huang, Y. Liu et al., Simulation and measurement of beam loading effects in magnetic alloy rf cavity of CSNS RCS. J. Phys. Conf. Ser. **2687**, 5 (2024). https://doi.org/10.1088/1742-6596/2687/5/052001
34. X. Li, H. Sun, C.L. Zhang et al., Design of rapid tuning system for a ferrite-loaded cavity. Radiat. Detect. Technol. Methods **5**, 324–331 (2021). https://doi.org/10.1007/s41605-021-00255-8
35. M. Yamamoto, M. Nomura, T. Shimada et al., Vacuum tube operation analysis under multi-harmonic driving and heavy beam loading effect in J-PARC RCS. Nucl. Instrum. Meth. A **835**(1), 119–135 (2016). https://doi.org/10.1016/j.nima.2016.08.028